Experiments in Fluids (2025) 66:71
https://doi.org/10.1007/s00348-025-03978-2

RESEARCH ARTICLE

Spatio-temporal characterization of the three-dimensional wave dynamics in falling film flows over rectangular corrugations

Andrea Düll[1] · Jannick Lehmann[1] · Marion Börnhorst[2] · Cihan Ateş[3] · Thomas Häber[4] · Olaf Deutschmann[1,4]

Received: 21 November 2024 / Revised: 21 January 2025 / Accepted: 23 January 2025

Abstract

Falling film flows over rectangular corrugations can exhibit intense time-oscillatory interfacial motion. This is of considerable interest for heat and mass transfer applications, where structured surfaces play a crucial role in process intensification. Our contribution relies on high-speed imaging and image processing based on an internally referenced light absorption method to obtain a full spatio-temporal characterization of the structure-induced wave evolution. After validating the customized experimental technique, particular emphasis is placed on identifying relationships between the steady and transient characteristics of aqueous falling film flows under operating conditions relevant to, e.g., falling film absorbers for CO_2 capture applications. The transient film instabilities are found to evolve from an initially steady film flow. In the investigated Reynolds number range, inertia-controlled liquid overshoot in wall-normal direction at the structure element's upstream edges plays a crucial role in the overall flow destabilization. The developed film flow can be decomposed into a steady and a time-oscillatory flow contribution. The former is characterized by a dominant two-dimensional wave shape with a primary wavelength matching that of the bottom contour, while the latter is more isotropic in shape. Nevertheless, both flow contributions are interconnected, with high oscillation intensities being usually accompanied by a strongly sloped steady base flow. In the context of surface structure optimization, the streamwise length scale of the steady interfacial ridge induced at an isolated structure element may serve as a predictor for identifying structure spacings that exhibit particularly strong transient flow destabilization.

1 Introduction

Falling film flows occur in a variety of technical applications involving heat and mass transfer. For instance, falling film evaporators find frequent application in the food industry (Cyklis 2022; Gourdon et al. 2015), falling film absorbers are often used in absorption refrigeration systems (Havestini and Ormiston 2020; Mortazavi et al. 2015) or for the investigation of CO_2 absorption (Zanfir et al. 2005; Zhang et al. 2018), and falling film reactors are a popular choice for highly exothermic gas–liquid reactions (Rößler et al. 2013). To improve the heat and mass transfer properties, the surface on which the liquid film flows is often structured (Åkesjö et al. 2019; Bontozoglou and Serifi 2008; Davies and Warner 1969). These surface structures can significantly affect the falling film hydrodynamics (Sayegh et al. 2022). Depending on the structure shape and dimensions, strong interfacial oscillations can be induced in the flow, as previously investigated using a spatially localized measurement technique (Düll et al. 2024). In order to optimize the employed surface structures, an in-depth understanding of the evolution of such transient film instabilities is necessary. This requires a coupled spatio-temporal characterization of the associated three-dimensional wave dynamics, which is the focus of our study.

✉ Thomas Häber
thomas.haeber@kit.edu

1 Institute for Chemical Technology and Polymer Chemistry, Karlsruhe Institute of Technology (KIT), Engesserstraße 20, 76131 Karlsruhe, Germany

2 Institute of Reaction Engineering and Catalysis, TU Dortmund University, Emil-Figge-Straße 66, 44227 Dortmund, Germany

3 Institute of Thermal Turbomachinery, Karlsruhe Institute of Technology (KIT), Kaiserstraße 12, 76131 Karlsruhe, Germany

4 Institute of Catalysis Research and Technology, Karlsruhe Institute of Technology (KIT), Hermann-von-Helmholtz-Platz 1, 76344 Eggenstein-Leopoldshafen, Germany

Published online: 11 March 2025

The measurement techniques commonly used to characterize thin film flows, both on flat and structured surfaces, can be grouped according to the dimensionality of the region of interest to which they are applied. Localized measurement systems, which monitor the liquid film thickness at a single measurement point, include chromatic confocal sensors (Collignon et al. 2021; Hu et al. 2021; Schröder 2019; Zhou et al. 2009), capacitance meters (Qi et al. 2019) or conductance probes (Mouza et al. 2000; Zhao et al. 2013). These point-wise measurement techniques allow high temporal resolution, but the full three-dimensional nature of the falling film flow remains elusive (Guzanov et al. 2018). Light sheet techniques, such as planar laser-induced fluorescence (PLIF), are frequently employed to image the evolution of the gas–liquid interface along an additional spatial coordinate (Charogiannis and Markides 2016; Zadrazil and Markides 2014). Here, particle imaging/tracking velocimetry (PIV/PTV) has additionally been employed to resolve internal flow structures and measure the local flow velocity within a two-dimensional cross section illuminated by the light sheet (Charogiannis and Markides 2019; Charogiannis et al. 2019; Guo et al. 2018; Schörner 2018; Wierschem et al. 2003; Zadrazil et al. 2014). Furthermore, in the context of heat and mass transfer applications, PLIF has been used to visualize local temperature (Collignon et al. 2021) and concentration (Kapoustina et al. 2019) fields within the liquid phase. To map the local film thickness along two spatial coordinates, i.e., along the liquid film's streamwise and spanwise direction, brightness-based LIF (BBLIF (Cherdantsev et al. 2023; Hann et al. 2016)) techniques (Argyriadi et al. 2006; Guzanov et al. 2018; Lu et al. 2017; Medina et al. 2022; Sayegh et al. 2022; Vlachogiannis and Bontozoglou 2002) or light absorption methods (Dupont et al. 2015; Mendez and Buchlin 2015; Njifenju et al. 2013; Özgen et al. 2002) find frequent application. Scanning light sheet techniques have also been used for this purpose (Al-Shamaa et al. 2023), and recently, magnetic resonance velocimetry was employed to visualize steady three-dimensional flow fields in falling films at the microscale (Saliba et al. 2024).

Based on the aforementioned experimental techniques, the evolution of two-dimensional traveling waves and their transition into three-dimensional wave structures beyond a certain inlet distance and Reynolds number limit was characterized in detail for falling film flows on smooth surfaces (Al-Sibai 2004; Guzanov et al. 2018). For mildly corrugated surfaces, the flow behavior is similar to that observed on smooth inclines, but deviations become significant at low inclination angles, with higher corrugation steepness, or increased inertia (Al-Shamaa et al. 2023). For falling film flows over rectangular corrugations, Vlachogiannis and Bontozoglou (2002) and Argyriadi et al. (2006) report the establishment of a steady three-dimensional flow pattern once the Reynolds number is increased beyond a peak value, at which the structure-induced two-dimensional interface deformation reaches maximum steepness. This pattern is first triggered far downstream, but extends over the entire flow domain above a certain Reynolds number threshold (Argyriadi et al. 2006). A similar phenomenon was found for sinusoidal corrugations (Al-Shamaa et al. 2023). While the reported three-dimensional flow patterns are mainly static in nature, they can significantly affect the overall flow dynamics due to the interaction of traveling disturbances with the underlying steady base flow (Argyriadi et al. 2006; Al-Shamaa et al. 2023; Vlachogiannis and Bontozoglou 2002). Also, for rectangularly corrugated surfaces, a reduction in the ridge width has recently been found to result in a considerable amplification of the transient film instabilities (Düll et al. 2024). Such unsteady flows are of high relevance for process intensification in heat and mass transfer applications (Al-Shamaa et al. 2023). However, few studies have been directed at characterizing the inherently three-dimensional nature of the structure-induced interfacial oscillations. Sayegh et al. (2022) applied a BBLIF technique with high spatial and temporal resolution to simultaneously record the local film thickness and interfacial velocity distributions for falling film flows over a smooth and a triangularly corrugated plate, with a focus on the effect of physio-chemical properties on wave evolution.

Our contribution relies on a similar experimental method and pursues two primary objectives. Firstly, we propose and validate an internally referenced light absorption technique to reduce commonly encountered measurement inaccuracies under wavy flow conditions. Secondly, we apply this customized experimental method to develop a deeper understanding of the evolution of structure-induced instabilities in aqueous falling film flows under conditions relevant to heat and mass transfer applications. In particular, falling film absorbers for CO_2 capture (Davies and Warner 1969) are selected as the exemplary application case. Arrays of rectangular ridges oriented perpendicular to the main flow direction are considered as a model structure geometry, and the effect of varying structure dimensions and Reynolds number is investigated in detail. By reconstructing the evolution of the gas–liquid interface in both space and time, we aim to complement the aforementioned works on steady three-dimensional flow patterns and extend our previous findings on the intensification of time-oscillatory interface motion by surface structure optimization (Düll et al. 2024), which were derived from a point-wise measurement technique. In this context, particular focus will be placed on elucidating relationships between the steady and transient falling film flow characteristics, within the applicable limits of the considered flow configuration.

2 Materials and methods

2.1 Experimental setup

Figure 1 shows the falling film test rig employed in this study. As it is based on the facility described in detail in Düll et al. (2024), only a brief overview is provided here, with a focus on the aspects most relevant to the customized optical measurement technique employed. The working fluid, consisting of deionized water with methylene blue dye (CAS: 61-73-4) dissolved at a concentration of 100mg/kg, is circulated by means of a micro-gear pump (LAB-ZP-9, Gather Industries). It passes through a settling chamber and a thin liquid distribution slit before entering the test section. The latter is inclined at $\alpha = 60.7°$ to the horizontal and has a length L (streamwise direction x) and width W (spanwise direction y) of 110mm and 50mm, respectively. Due to the finite plate width, the experimental measurements can be influenced by sidewall effects. As discussed in our previous study (Düll et al. 2024), these effects are primarily observed for the smooth reference plate. In contrast, they are significantly reduced in the case of structured backplates, where the wavelength of the observed interfacial oscillations is much smaller than the plate width. This is exemplarily visualized in Fig. 15 (Appendix A).

To study the effect of surface structure modification on the film flow characteristics, the falling film wall is easily interchangeable. The structured surfaces considered here are selected from those studied in our previous work (Düll et al. 2024), chosen to ensure that different flow behaviors can be observed. They consist of arrays of rectangular structure elements oriented perpendicular to the main flow direction, as visualized in detailed view (b) in Fig. 1. In addition to a smooth reference plate, backplates with varying structure distance $D_s/\text{mm} \in \{2, 3, 4, 6, 8\}$ at structure heights around $H_s \approx 0.4$ mm as well as backplates with varying structure height $H_s/\text{mm} \in \{0.22, 0.45, 0.81, 1.2\}$ at constant structure distance $D_s = 4$ mm are considered. The streamwise length of an individual structure element is kept constant at $L_s = 0.7$ mm. These geometric dimensions are average values calculated from post-manufacturing line scan measurements with a chromatic confocal point sensor. The corresponding manufacturing accuracy was determined to be in the order of ± 30 µm. To ensure optical accessibility, the backplates are machined from acrylic glass sheets (Plexiglas XT, Röhm). The test section is backlit by three white LED lamps (Constellation 120E, Veritas) during image acquisition with a CMOS high-speed color camera (XStream mini 3520, IDT) equipped with a 50 mm objective lens. As with most conventional CMOS or CCD digital cameras, a Bayer filter is integrated into the employed high-speed camera to produce colored images. While this limits the image resolution to features larger than a cell of 2 × 2 photosites forming the Bayer filter's mosaic pattern, it allows for the use of only one digital camera to capture light intensities in different wavelength ranges, eliminating the need for two synchronized cameras with additional filter optics. Depending on the application, further simplification of the experimental setup could be achieved by using widely available low-speed imaging equipment. Two additional 1-mm-thick diffuser plates (colourLED No. 11, BWF) are placed in front of the light sources to enhance the illumination homogeneity. To evaluate the accuracy of the optical measurement technique, this work relies on point-wise film thickness measurements performed in our previous work (Düll et al. 2024) using a chromatic confocal point sensor (CHRocodile 2 S, Precitec).

2.2 Experimental procedure and operating conditions

For each of the structured surfaces indicated in Fig. 1, falling film flow is studied at six distinct liquid loads by varying the volume flow rate $\dot{V}$ supplied by the pump. The corresponding volumetric flow rates per unit width q and Reynolds numbers

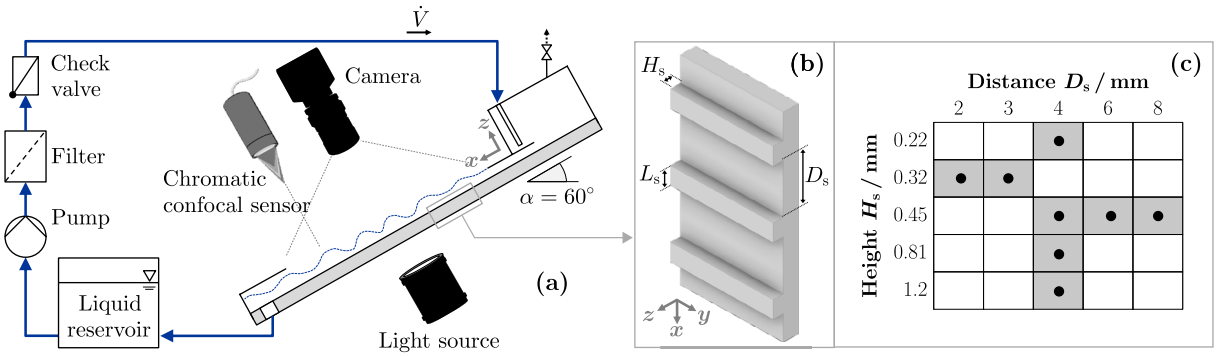

Fig. 1 Experimental setup (**a**) and detailed view (**b**) of the investigated surface structure geometry. The structure distance (D_s) and height (H_s) combinations studied here are indicated in the matrix representation (**c**) by gray shading

Re (Schagen 2014) are given in Eqs. 1 and 2, where W and ν are the test section's width and the working fluid's kinematic viscosity, respectively.

$$q = \frac{\dot{V}}{W} \in \{2.27, 2.76, 3.25, 3.74, 4.23, 4.72\} \times 10^{-4} \mathrm{m}^2/\mathrm{s} \tag{1}$$

$$Re = \frac{q}{\nu} \in \{232, 282, 332, 382, 432, 482\} \tag{2}$$

Prior to the start of an experimental run, a series of ten reference images is taken of the dry backplate. These are used to determine the region of interest during image processing. Afterward, the liquid flow rate is increased up to its maximum value to ensure full plate wetting and an initially homogeneous liquid distribution. In a first experimental phase, the liquid flow rate is then progressively reduced, and at each of the previously indicated Reynolds number setpoints, images of the falling film flow are captured with a frequency of 1200 Hz and an exposure time of 70 µs over a time period of 10s. This is followed by a second (third) experimental phase, in which data acquisition is carried out at the same *Re* values, but with the liquid flow rate gradually increased (reduced). This procedure yields three temporally separated measurement repetitions for each experimental setpoint.

All flow experiments are conducted in a climate-controlled laboratory at an average ambient temperature of $\overline{T} = 21\,^{\circ}\mathrm{C}$. To calculate characteristic film properties, the liquid density, kinematic viscosity and surface tension are assumed to be $\rho = 997.99\,\mathrm{kg/m^3}$, $\nu = 10^{-6}\mathrm{m}^2/\mathrm{s}$ and $\sigma = 72.59 \times 10^{-3}\mathrm{N/m}$, respectively (Wagner and Kretzschmar 2013).

2.3 Image processing and camera calibration

The image processing routine applied in this study is derived from the light absorption method (Clark 2002). The latter relies on Beer–Lambert's law, which relates the local film thickness to the amount of light being absorbed from a light ray as it passes through the liquid layer (Mendez and Buchlin 2015). To derive light absorbance values from the locally transmitted light intensity, the corresponding incident light intensity must be known as a reference value (Mouza et al. 2000). The latter is commonly extracted from reference images of the dry solid surface (Mendez and Buchlin 2015). However, for wavy film flows such as the ones encountered in this study, increased curvature of the gas–liquid interface can lead to a misalignment of local background inhomogeneities between the reference image and the images captured of the liquid film. This is particularly relevant for the structured backplates used here, as the manufacturing process leaves behind slightly visible milling traces, and pronounced light intensity variations can occur in the vicinity of the structure element's sharp edges. Moreover, irrespective of the properties of the solid surface, local light reflection and refraction at the gas–liquid interface can introduce additional inaccuracies in case of high interfacial slopes (Clark 2002; Mendez and Buchlin 2015). These optical distortions limit the accuracy of many commonly used image-based film thickness measurement techniques, as discussed in detail by Cherdantsev et al. (2023).

To minimize the potential for experimental errors due to the aforementioned factors, this study uses a broadband light source instead of a monochromatic one (see Fig. 2a),

allowing for the use of a pixel-wise internal reference instead of an external reference for the incident light intensity. As shown in Fig. 2b, methylene blue absorbs light primarily in the wavelength range $\lambda = 550 - 700$ nm. The increase in liquid film thickness, i.e., the increase in the amount of red-absorbing dye species, is thus well captured by the camera's red color channel (see Fig. 2c). It results in a decrease in the detected light intensity I_{red}. In contrast, the dye's light absorption in the wavelength range of $\lambda = 400 - 550$ nm is negligible, and the light intensity detected by the camera's blue color channel I_{blue} is therefore significantly less affected by changes in liquid film thickness. The ratio of these two values

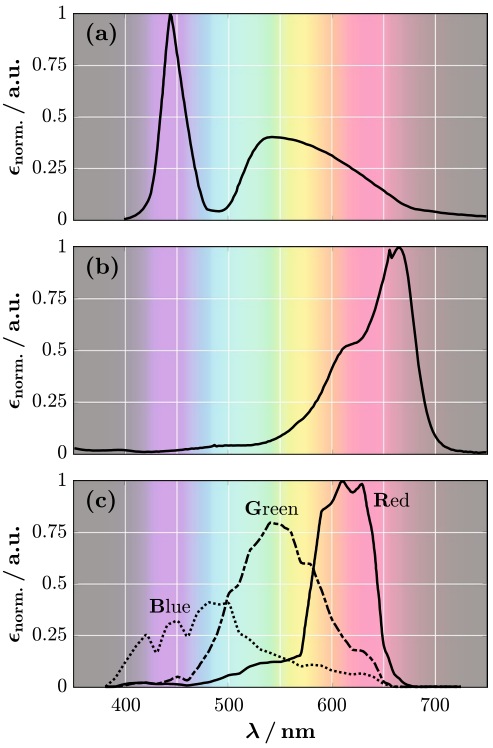

Fig. 2 Spectral curves of the light emitted by the light source (**a**), absorbed by the dye (**b**) and captured by the camera's three color channels (**c**). The underlying raw data correspond to data from Imaging Solutions (2024), Prahl (2017) and Integrated Design Tools, Inc. (IDT), respectively

can thus serve as an internally referenced indicator for the local film thickness h, as formulated in Eq. 3.

$$\frac{I_{\mathrm{red}}}{I_{\mathrm{blue}}} = f(h) \quad \text{with} \quad \left|\frac{\partial I_{\mathrm{red}}}{\partial h}\right| \gg \left|\frac{\partial I_{\mathrm{blue}}}{\partial h}\right| \tag{3}$$

The advantage of such an internal reference is exemplified in Fig. 16 (Appendix B), which compares the distribution of the gray scale intensity to that of the red-to-blue color ratio for a sample image with constant liquid film thickness. The latter is much more homogeneously distributed, demonstrating that the need for an additional external reference to correct for potential error sources, such as non-uniform illumination of the measurement plane or vignetting effects, is eliminated. It should be noted that the occurrence of total internal reflection would nevertheless prevent reliable measurement results. However, the slope of the gas–liquid interface with respect to the measurement plane is generally well below 45°, as determined by preliminary tests, making total internal reflection a highly localized phenomenon in both space and time. Similarly, errors due to the dependence of the refractivity and the reflectivity at the phase boundary on the wavelength are largely negligible under the conditions used here and are in the low single-digit percentage range of the measured film thickness.

An initial calibration step is required to determine the exact relationship between the relative color intensity $I_{\mathrm{red}}/I_{\mathrm{blue}}$ and the liquid film thickness h. For this purpose, thin stainless steel shims (vario-plate, peel-plate GmbH) are used to create precise gaps in the range of $0.1 - 4$ mm between two acrylic glass plates. These gaps are filled with aqueous dye solution, and a series of ten calibration images is captured for every liquid layer thickness using the same camera settings and backlighting configuration as for the flow measurements. In a subsequent image processing step, the local color intensity ratios are extracted pixel-wise and averaged over a region of interest of 604×340 pixels, as well as over the ten separate calibration images. The spatial variation in the color intensity ratio across the calibration plane is small compared to the calculated mean values, with relative standard deviations in the range of 1−3% for film thicknesses below $h = 2$ mm and in the range of 3−7% for higher film thicknesses up to $h = 4$ mm. The determined calibration points are visualized in Fig. 3. They can be fitted by Eq. 4.

$$\frac{I_{\mathrm{red}}}{I_{\mathrm{blue}}} = 0.07816 + 0.9465 \cdot \exp\left(\frac{-1.802\,h}{\mathrm{mm}}\right) \tag{4}$$

As shown in Fig. 3, the optical measurement method is highly sensitive to changes in film thickness up to $h \approx 2$ mm, while its sensitivity is significantly reduced for thicker films. Theoretically, the measurement uncertainty for increased film thicknesses could be improved by reducing the dye concentration. However, this would inevitably lead to an increase in measurement uncertainties for thinner films (Mendez et al. 2016).

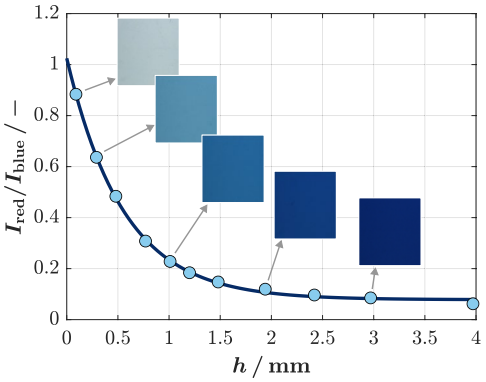

Fig. 3 Ratio between the light intensities captured by the camera's red and blue color channel $I_{\mathrm{red}}/I_{\mathrm{blue}}$ as a function of the liquid layer thickness h. Experimental measurement points (circles) and the fitted curve from Eq. 4 (solid line) are shown alongside representative raw images

To evaluate the main flow experiments, local red-to-blue color intensity ratios $I_{\mathrm{red}}/I_{\mathrm{blue}}$ are extracted from the captured images at each pixel of a predefined region of interest. Subsequently, the corresponding film thickness values h are determined based on an interpolated calibration curve. To convert from pixel coordinates to physical coordinates for further data analysis, an additional spatial calibration is performed using the image of a printed checkerboard pattern, from which an average image resolution of 63.7 µm\px is determined in both streamwise (x) and spanwise (y) directions.

2.4 Data evaluation

The previously described image processing routine yields a spatio-temporal film thickness distribution $h(x, y, t)$. Using the coordinate system visualized in Fig. 4, the elevation of the gas–liquid interface $z_h(x, y, t)$ is determined from this film thickness distribution by subtracting the surface structure height H_{s} at x-positions located within the trenches between individual structure elements and subtracting zero elsewhere.

In the discussion section, the film thickness h will be employed for comparing our customized measurement method with a commercial technique (Sect. 3.1), as it is the property directly obtained from image processing. It is a locally referenced value without a global reference frame. The interface elevation z_h will serve as the target variable in all subsequent sections (Sect. 3.2–3.4), where spatial flow distributions are analyzed. It is referenced to the global coordinate system shown in Fig. 4, whose origin in z direction is located on the top of the structure elements.

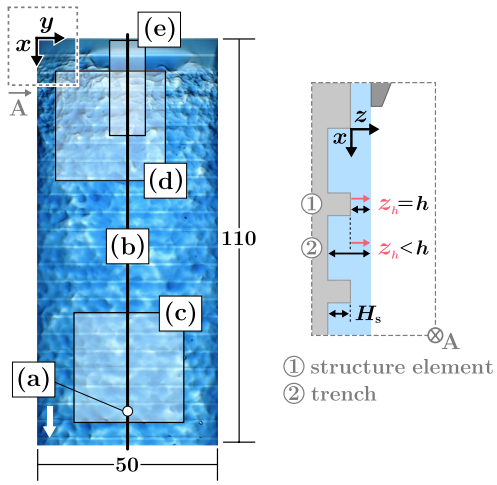

Fig. 4 Top view of the regions of interest considered for quantitative data analysis. The origin of the employed coordinate system as well as the definition of the film thickness h and interface elevation z_h is shown in the schematic side view A

Negative values thus indicate that the gas–liquid interface has penetrated into the trenches between consecutive structure elements. Experimental results extracted from regions of interest of varying spatial dimensionality are discussed. As can be taken from Fig. 4, these include a 0D point (a), a 1D line (b) as well as three 2D rectangles (c)-(e). Key statistical parameters considered for quantitative data evaluation include the temporal mean of the film thickness h or interface elevation z_h (notation $\overline{X}$ for a generic variable X) as well as the standard deviation s_X or interquartile range IQR_X of their spatial or temporal distributions. The latter two can be interpreted as measures for the waviness of the falling film flow, with higher values indicating stronger interface deformation.

3 Results and discussion

In the following sections, the spatio-temporal wave evolution in aqueous falling film flows over rectangular corrugations is discussed for regions of interest of increasing spatial dimensionality. In all cases, particular emphasis is placed on elucidating relationships between steady and transient flow characteristics. In Sect. 3.1, the experimental results obtained at a 0D measurement point on the basis of our customized light absorption technique are compared to measurements with a commercial chromatic confocal sensor. After this initial validation step, the evolution of transient film instabilities along a 1D line in the streamwise direction is discussed in Sect. 3.2, while the three-dimensional characteristics of the evolving waves are examined through analysis of a 2D rectangular region of interest in Sect. 3.3. Finally, in Sect. 3.4, characteristic length scales of steady interfacial deformations induced by quasi-isolated structure elements are extracted and related to optimal surface structure dimensions for intensifying the observed interfacial oscillations.

3.1 Comparison of different measurement techniques

To assess the suitability of the customized light absorption method for capturing the dynamic film flow characteristics, the experimental results obtained with this technique are compared against measurements taken with a commercial chromatic confocal point sensor. Details on the latter can be found in our previous work (Düll et al. 2024). The analysis is performed at the single spatial measurement point (a) indicated in Fig. 4. It is centered along the width of the plate ($y = 25$ mm) and located at a distance of $x \approx 100$ mm from the liquid distributor. The latter is slightly adjusted depending on the structure distance D_s of each backplate, to ensure that the measurement point remains centered between two consecutive structure elements. Figure 5a and bshows parity plots of the mean film thickness $\overline{h}$ and film thickness standard deviation s_h of the local film thickness time series $h(t)$ for all investigated structure geometries and Reynolds numbers. The values determined based on the chromatic confocal sensor measurements and the customized light absorption technique are indicated on the abscissa and ordinate, respectively. For readability, the mean values calculated from the nine experimental repetitions conducted for the former and the three experimental repetitions conducted for the latter are shown instead of single measurement points. As can be seen from the figures, the experimental results from both measurement methods are in good agreement, with no discernible systematic discrepancies. This applies to both static and dynamic flow properties, as represented by the mean film thickness $\overline{h}$ and the film thickness standard deviation s_h, respectively. Stronger deviations are primarily observed for lower liquid loads ($Re \leq 282$), which can be caused by flow inhomogeneities due to local dewetting effects occurring below a certain Re threshold. In such cases, the local liquid distribution and flow dynamics can vary distinctly between two experimental runs.

Figure 6provides a more detailed comparison for a constant Reynolds number of $Re = 482$. In the figure, the film thickness standard deviation s_h is plotted as a function of the structure distance-to-height ratio D_s/H_s. Sensor measurements for a more extensive range of structure dimensions (open symbols) are shown in addition to the experimental results derived from our light absorption method (filled symbols). Additionally, a comparison

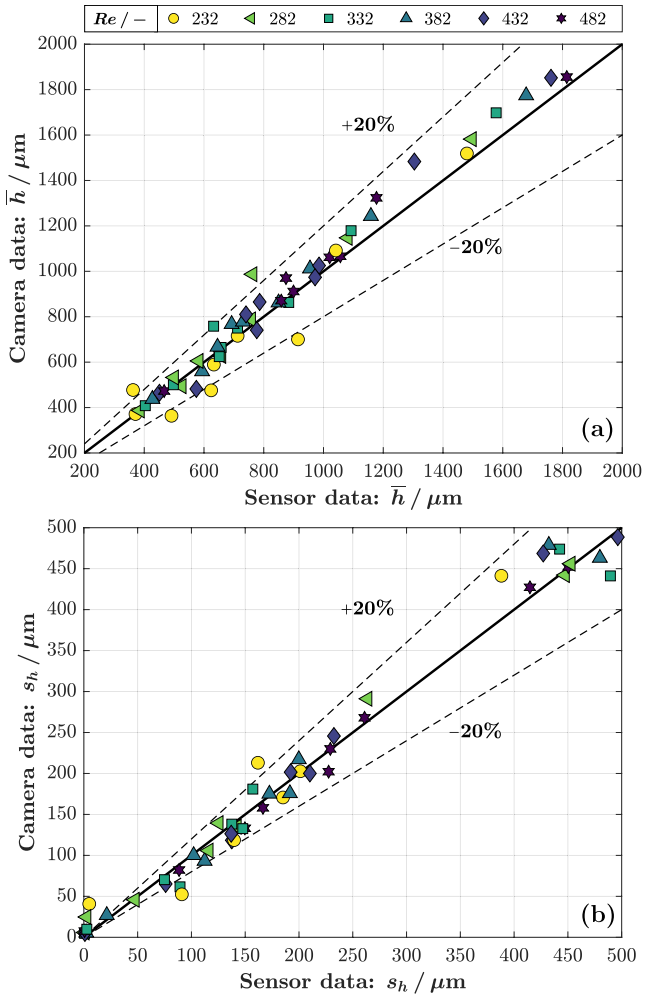

Fig. 5 Parity plots of the mean film thickness $\overline{h}$ (**a**) and film thickness standard deviation s_h (**b**) determined from the local time series $h(t)$ at $x \approx 100$ mm and $y = 25$ mm (measurement point (**a**) in Fig. 4). The identity line (solid) and ±20% error limits (dashed) are indicated

between two exemplary film thickness distributions is provided. Film flow over the smooth reference plate remained quasi-smooth in all experimental cases due to the relatively low plate length ($s_h < 8\mu\text{m}\,\forall\,Re$) and is therefore not considered further. On the one hand, with respect to the suitability of the customized experimental technique, its repeatability and accuracy are well sufficient to detect deviations between different structure geometries. Exemplarily, for $D_s = 4$ mm and $H_s = 0.45$ mm, the absolute deviation between three consecutive experimental runs is in the order of $\Delta s_h \approx 10$ µm. On the other hand, with respect to the transient film flow characteristics, an optimal structure distance or structure distance-to-height ratio can be determined for each structure height, at which particularly strong interfacial oscillations are induced in the flow and the film thickness standard deviation s_h reaches its maximal value. In the following, this structure distance will be

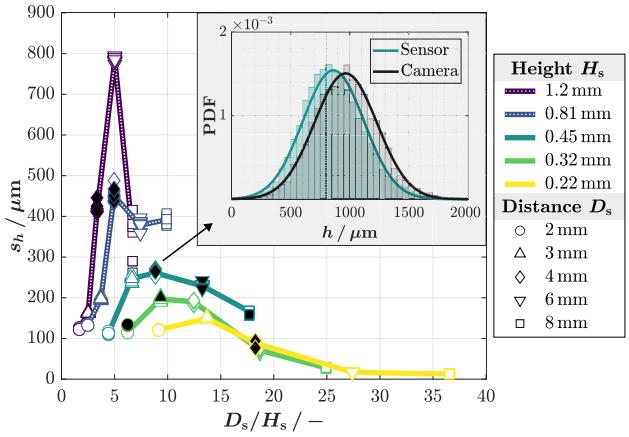

Fig. 6 Standard deviation s_h determined for the local film thickness time series $h(t)$ at $x \approx 100$ mm and $y = 25$ mm (measurement point (**a**) in Fig. 4) for structured surfaces with systematically varied structure distance D_s and height H_s. Sensor measurements (nine repetitions) are indicated by open symbols and interpolated by solid lines, and results based on the customized light absorption method (three repetitions) are indicated by filled symbols. Exemplary film thickness distributions are shown in the form of probability density functions (PDFs). $Re = 482$

referred to as the 'optimal structure distance' D_s^*. However, it must be emphasized that D_s^* is determined from a discrete set of values, and the true global optimum could lie between the investigated points. The observed intensification of interfacial oscillations is of particular relevance for heat and mass transfer applications, as discussed in greater detail in our previous study (Düll et al. 2024). Using the light absorption technique validated for our specific application, the following sections focus on developing a detailed understanding of the observed transient flow destabilization and the associated wave characteristics. Instead of the previously considered film thickness h, the derived interface elevation z_h (see Fig. 4) will be used as the target variable to describe the spatial flow distributions in an undistorted manner. The standard deviation and interquartile range calculated from the temporal distributions of either property are identical ($s_{h(t)} = s_{z_{h(t)}}$ and $IQR_{h(t)} = IQR_{z_{h(t)}}$).

3.2 Evolution of transient film instabilities

To understand how the observed transient film instabilities emerge over the length of the falling film wall, the spatio-temporal distribution of the gas–liquid interface $z_h(x,t)$ is analyzed along a line in streamwise (x) direction. This one-dimensional region of interest is centered across the plate width ($y = 25$ mm) and is marked by label (b) in Fig. 4. The evaluation presented below focuses on three different structured surfaces with structure heights of $H_s \approx 400$ µm, for which distinctly different flow behaviors are expected based on the point-wise measurement results (see Fig. 6).

Specifically, structure arrays with structure distances or distance-to-height ratios below ($D_s = 2$ mm, $D_s/H_s = 6.3$), at ($D_s = 4$ mm, $D_s/H_s = 8.9$) and above ($D_s = 8$ mm , $D_s/H_s = 17.8$) the respective optimal value for maximized interfacial oscillatory motion are considered. Representative raw image snapshots from the considered experimental cases are shown in Fig. 7.

The corresponding spatio-temporal flow distributions are summarized in Fig. 8 (left column), where the elevation of the gas–liquid interface $z_h(x,t)$ is plotted as a function of the flow distance x.

Instead of visualizing the position of the gas–liquid interface individually for each of the 12,000 time steps within an experimental run time of 10 s, local point densities are calculated on a binned grid with a resolution of 63.7×20 µm^2 (abscissa×ordinate). The resulting field is visualized using a colormap, where darker coloring indicates a higher probability of the gas–liquid interface being at a given position. For quantitative comparison, the mean values $\bar{z}_h$ and standard deviations s_{z_h} of the film thickness time series $z_h(t)$ evaluated at each discrete flow distance x are additionally shown in Fig. 8 (right column).

Assessing first the transient flow destabilization for varying structure distances D_s at a constant Reynolds number of $Re = 482$ in Fig. 8a–c, it becomes evident that the particularly strong interfacial oscillations, which were identified for the intermediate structure distance $D_s = 4$ mm based the point-wise flow evaluation (see Fig. 6), are induced already at comparably low flow distances. They can be observed across nearly the entire plate length with consistently strong intensity, as quantified by the standard deviation of the local surface elevation's time series (see Fig. 8 (b2)). The latter is particularly high directly after each structure element but slightly decreases within the trench before reaching the edge of the next structure element, suggesting that structure-induced liquid overshoot in wall-normal direction plays an important role in the overall flow destabilization. This phenomenon is less pronounced for the lower ($D_s = 2$ mm) or higher ($D_s = 8$ mm) structure distances considered. In case of the former, the narrow structure spacing keeps the gas–liquid interface from penetrating into the trenches between consecutive structure elements, as visualized in Fig. 8 (a1). In case of the latter, the interface deformations induced at consecutive structure elements are spaced too far apart to interact strongly, as seen in Fig. 8 (c1).

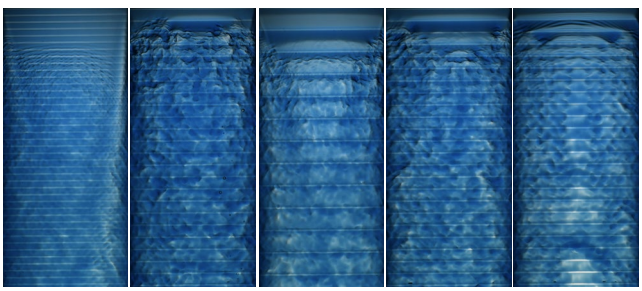

Fig. 7 Representative raw images corresponding to the experimental cases shown in Fig. 8 with matching letter indices. Video animations of (**a**–**e**), slowed down by a factor of 100, are provided in Online Resources 1–5

The effect of Reynolds number on the evolution of transient film instabilities is visualized in Fig. 8a, d and e for a constant structure distance of $D_s = 4$ mm. With decreasing Reynolds number, the structure-induced interfacial oscillations become generally less pronounced, and their onset is shifted to higher flow distances. This indicates that the previously described structure-induced liquid overshoot and the associated transient film flow destabilization are primarily controlled by inertial forces. It should be noted that the strong interfacial motion and high probability of the gas–liquid interface being in close proximity to the solid surface, as observed for the lowest considered Reynolds number $Re = 282$, are related to temporary dewetting effects (see Fig. 7e). These lead to a distortion of the local flow statistics.

Irrespective of the structure distance, height or Reynolds number, i.e., regardless of the intensity of the developed interfacial oscillations, the transient film instabilities evolve from an initially steady film flow. This transition occurs gradually in the case of low structure heights ($H_s \leq 0.32$ mm) or structure distances well below or above the respective optimal value ($D_s = 2$ mm, $D_s = 8$ mm). In contrast, for high structure heights ($H_s \geq 0.45$ mm) and structure distances close to the optimal value ($D_s = 4$ mm, $D_s = 6$ mm), particularly pronounced liquid overshoot can result in a very abrupt onset of strong interfacial oscillations. This phenomenon is especially prevalent at higher Reynolds numbers, where inertial forces are particularly strong, while local oscillatory behavior may be damped out at lower Reynolds numbers (see Fig. 8e, $x \approx 5$ mm).

While the exact flow behavior, and particularly that in the vicinity of the liquid inlet ($x \to 0$), may be affected by the experimental configuration, the above analysis demonstrates that inertial effects and the steady flow properties play a crucial role in the evolution of transient film instabilities. The relevance of the steady interface deformation was also emphasized by other authors with respect to the suppression of traveling waves in falling film flows over symmetrical rectangular or sinusoidal corrugations (Al-Shamaa et al. 2023; Vlachogiannis and Bontozoglou 2002). The following section will therefore focus on analyzing the spatial characteristics of both the transient interfacial waves and the underlying steady film flow.

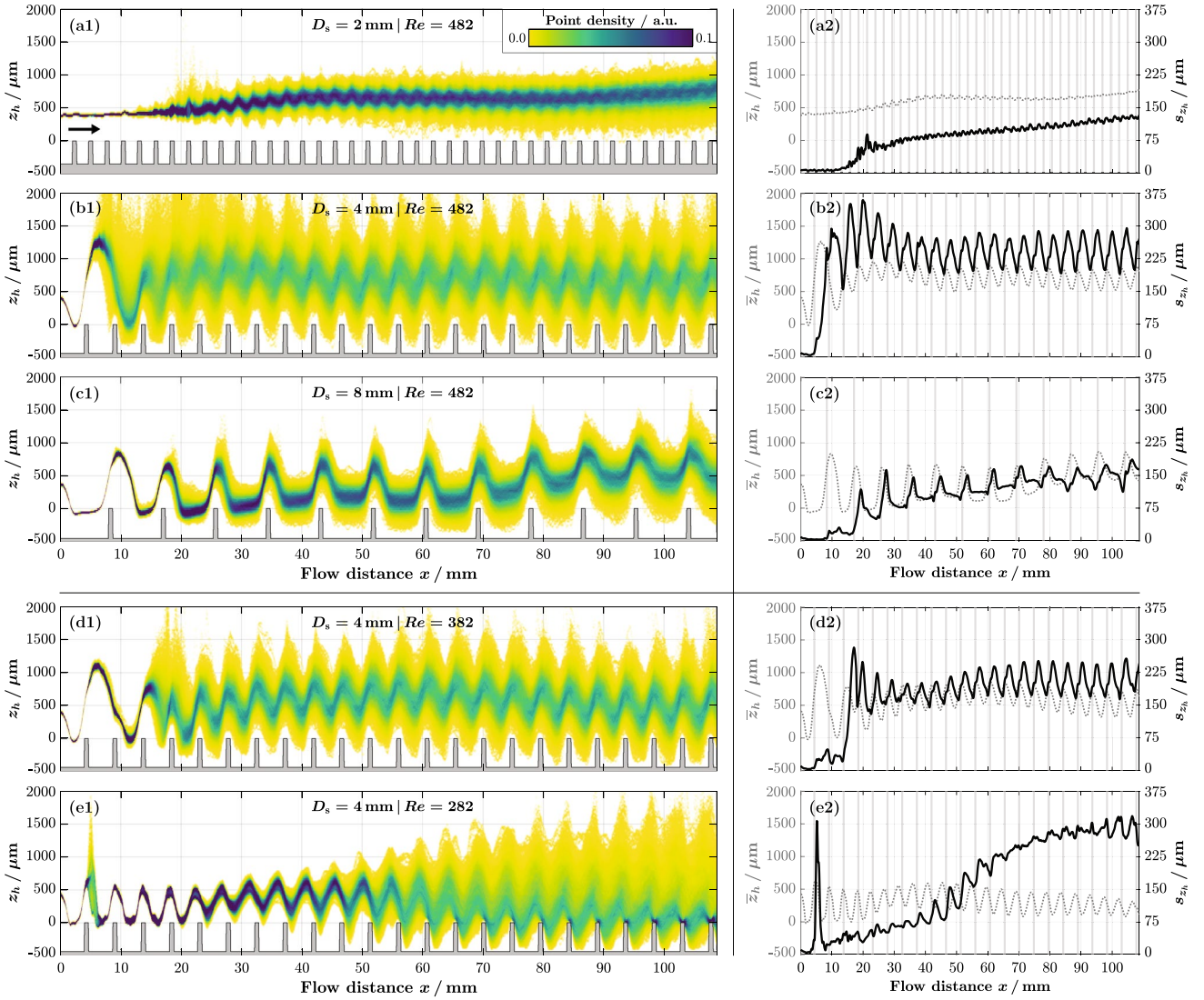

Fig. 8 Spatio-temporal evolution of the elevation of the gas–liquid interface $z_h(x,t)$ as a function of the flow distance x at constant $y = 25$ mm. Results for different structure distances D_s (**a1**, **b1**, **c1**) and Reynolds numbers Re (**d1**, **e1**) are shown. The colormap indicates local point densities calculated from the superposition of the 12,000 individual spatial profiles captured over a time period of 10s. The flow direction is indicated by an arrow in subfigure (**a1**). The mean values $\bar{z}_h(x)$ and standard deviation $s_{z_h}(x)$ of the local time series $z_h(t)$ at each discrete flow distance x are shown in the right column (index 2), where the positions of the elevated structure elements are indicated by gray shading

3.3 Three-dimensional wave characteristics

To evaluate the spatial three-dimensional characteristics of the transient waves independent of the steady interface deformation, the overall film flow (z_h) is decomposed into a steady ($\bar{z}_h$) and a time-oscillatory contribution (z'_h). The former is determined by temporally averaging the local film thickness or corresponding elevation of the gas–liquid interface over the entire experimental runtime of 10s (12,000 images). The latter is subsequently obtained by subtracting the steady interface profile from a representative profile captured at a single time instance. In the following, the main findings are first illustrated using a representative experimental case, before general conclusions are discussed.

An exemplary result of a temporal flow decomposition is shown in Fig. 9 for a structure distance of $D_s = 4$ mm, a structure height of $H_s = 0.45$ mm and a Reynolds number of $Re = 382$, for which strong transient flow destabilization was previously observed (see Fig. 8d).

Figure 9a represents the spatial elevation of the gas–liquid interface $z_h(x,y)$ for the overall falling film flow, while

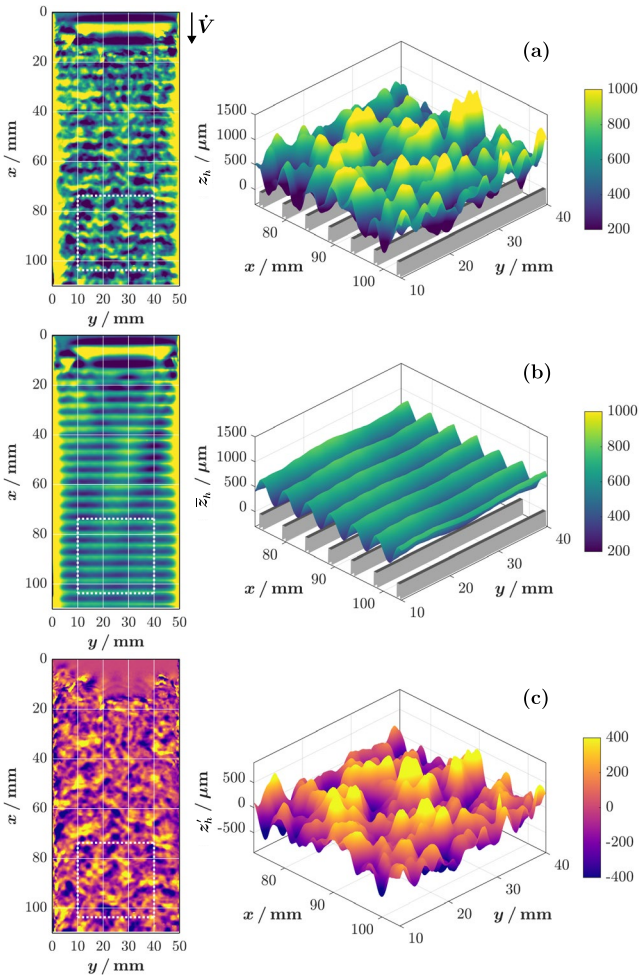

Fig. 9 Spatial distribution of the interface elevation over the entire measurement domain (left) and in a zoomed-in region of interest (right). The fields are visualized (**a**) for the overall film flow $z_h(x, y)$ as well as (**b**) for the decomposed steady contribution $\bar{z}_h(x, y)$ and (**c**) for the oscillatory contribution $z'_h(x, y)$. A video animation of (**a**), slowed down by a factor of 100, is provided in Online Resource 6. $D_s = 4$mm, $H_s = 0.45$mm and $Re = 382$

the corresponding steady and oscillatory flow contributions $\bar{z}_h(x, y)$ and $z'_h(x, y)$ are visualized in Figs. 9b and c, respectively. For each case, the results are visualized over the entire measurement domain (left) as well as in a zoomed-in region of interest of 30×30 mm (right), whose position is indicated by dashed white squares. The latter starts at a flow distance of $x = 73.8$ mm and is centered across the plate width (y-coordinate). It is visualized by label (c) in Fig. 4. The oscillatory wave statistics calculated from the spatial flow distribution in this zoomed-in region of interest at a single time instance are in good agreement with the values determined from the temporal flow evolution at the localized measurement point from Sect. 3.1 (see Fig. 17 in Appendix C).

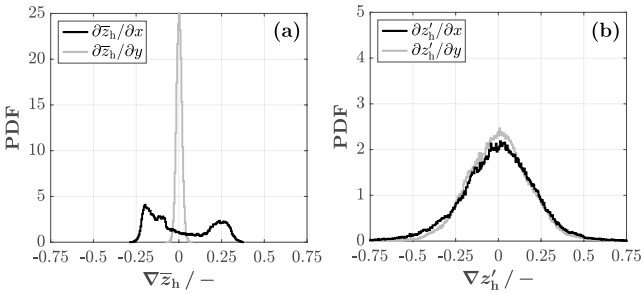

Fig. 10 Probability density functions (PDFs) of the spatial gradient fields $\nabla\bar{z}_h(x, y)$ and $\nabla z'_h(x, y)$ calculated for the steady (**a**) and oscillatory (**b**) flow contributions over the region of interest (**c**) in Fig. 4 (also indicated by dashed white rectangles in Fig. 9). $D_s = 4$ mm, $H_s = 0.45$ mm and $Re = 382$

By comparing the individual spatial distributions in Fig. 9, it becomes evident that the steady and oscillatory flow contributions exhibit distinct spatial characteristics. The oscillatory waves appear to be isotropic in both the streamwise and spanwise directions (see Fig. 9c). By contrast, the underlying steady base film is characterized by a dominant two-dimensional wave pattern oriented parallel to the structure elements (see Fig. 9b). This behavior is quantitatively reflected in the interface elevation's spatial gradient ∇z_h. The gradient fields calculated for the steady and oscillatory flow contributions in the zoomed-in region of interest are visualized in Fig. 18 in Appendix D, and the probability density functions of the corresponding gradient distributions are shown in Fig. 10.

For the steady flow contribution, the absolute values of the gradient in the flow direction (x) are significantly larger than those in the spanwise direction (y). In contrast, both gradient distributions are comparable in shape and magnitude for the oscillatory part, evidencing the isotropic nature of the dynamic structure-induced wave pattern, despite the fact that the solid bottom contour itself is non-isotropic.

These observations are not unique to the exemplary case presented above, but can be generalized to all experimental conditions investigated in this study. Firstly, the steady flow contribution is generally characterized by a dominant wave shape in the streamwise direction. As can be taken from Fig. 11a and b, its primary wavelength $\Delta x_{\mathrm{crest+trough}}$ matches that of the underlying structure elements $\lambda_s = D_s + L_s$.

At the lowest investigated Reynolds number $Re = 232$, the crest size remains roughly constant at $\Delta x_{\mathrm{crest}} \approx 2$ mm and the corresponding trough size $\Delta x_{\mathrm{trough}}$ increases linearly with increasing structure distance D_s (see Fig. 11a). In contrast, for the highest investigated Reynolds number $Re = 482$, a pronounced expansion of the crest size can be observed up to $D_s \leq 6$ mm (see Fig. 11b). Thus, for $D_s \leq 6$ mm, the steady interface deformation induced at an individual structure

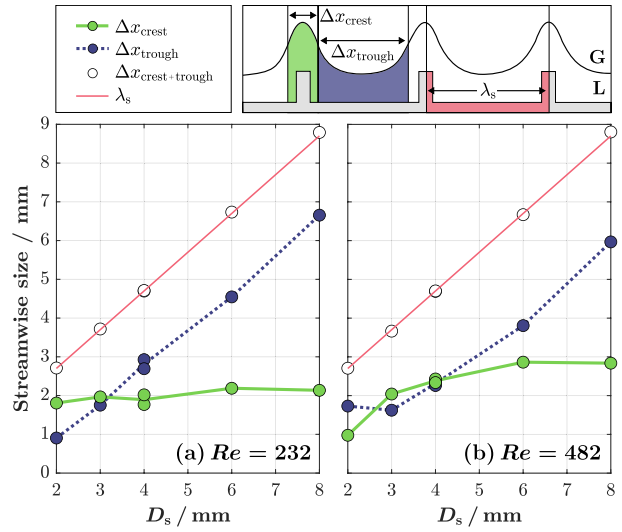

Fig. 11 Streamwise crest size Δx_{crest}, trough size $\Delta x_{through}$ and overall wavelength $\Delta x_{crest+trough}$ of the steady interface deformation $\bar{z}_h$ as a function of structure distance D_s for two different Reynolds numbers Re. The corresponding wavelength of the solid substrate λ_s is also plotted. Results are shown only for $H_s \leq 0.45$ mm

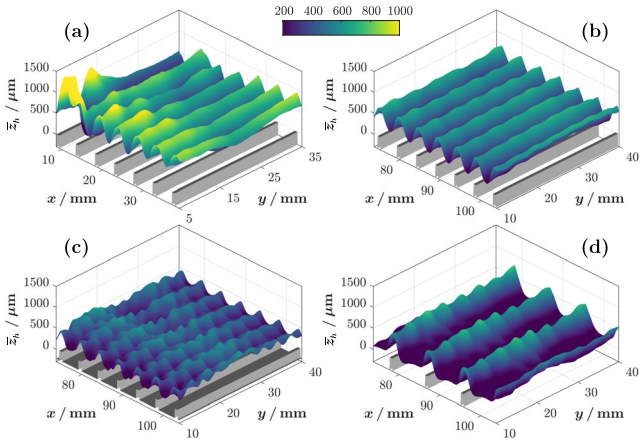

Fig. 12 Spatial distribution of the steady interface elevation $\bar{z}_h(x, y)$. Compared with the profile from Fig. 9b, the presented results are evaluated **a** from a region of interest located further upstream and closer to the sidewalls (rectangle (d) in Fig. 4), **b** for a lower Reynolds number $Re = 332$, **c** for a lower structure height $H_s = 0.2$ mm and **d** for a higher structure distance $D_s = 8$ mm

element is affected by the presence of its neighboring corrugations. As no further increase in the crest size is observed for a structure distance of $D_s = 8$ mm, such spaced structure arrays can be considered quasi-isolated. They are analyzed in more detail in Sect. 3.4 to extract characteristic length scales.

Secondly, the oscillatory flow contributions generally exhibit spatial characteristics that differ significantly from those of the steady flow. Intense time-oscillatory motion typically occurs when the underlying steady base film is strongly sloped, i.e., when the steady interface elevation exhibits particularly high spatial gradients (see Fig. 19a in Appendix D). This is another indicator of the interconnection between steady and oscillatory flow characteristics.

Lastly, while the above discussion focused on the dominant two-dimensional shape of the steady flow contribution, it should be mentioned that, under certain conditions, regions of steady three-dimensional flow patterns are also observable. Exemplary cases are shown in Fig. 12, and the corresponding spatial gradient fields are provided in Fig. 20 in Appendix D.

In contrast with the inherently three-dimensional time-oscillatory interface motion that spans almost the entire measurement domain (see Fig. 9a and c), the observed steady wave patterns are typically more localized effects. This contrasts with the observations of Vlachogiannis and Bontozoglou (2002) but is consistent with those of Al-Shamaa et al. (2023). The steady three-dimensional wave patterns become more prevalent when the oscillatory interface deformation is weak, as quantified in Fig. 19b in Appendix D. They occur, for example, at low flow distances in proximity to the sidewalls (Fig. 12a), at reduced Reynolds numbers (Fig. 12b), for low structure heights (Fig. 12c) and for structure distances above the optimal value (Fig. 12d). This finding supports the link between the occurrence of three-dimensional steady wave patterns in falling films and a general flow stabilization, as observed in previous studies (Al-Shamaa et al. 2023; Vlachogiannis and Bontozoglou 2002) with respect to the suppression of traveling waves.

3.4 Characteristic length scales for quasi-isolated corrugations

The steady and time-oscillatory flow contributions are interconnected, as evidenced by the evolution of the transient film instabilities from an initially steady film (Sect. 3.2) and the occurrence of intense oscillatory interface motion for strongly sloped steady base flows (Sect. 3.3). This section aims to apply this observation to surface structure optimization in the context of heat and mass transfer applications. Specifically, the focus is on analyzing whether characteristic length scales extracted from steady interface profiles may be used as estimators for surface structure dimensions that induce particularly strong transient film instabilities.

The analysis is based on the quantification of the interface deformation induced by a single structure element. The corrugated surface with a structure distance and height of $D_s = 8$ mm and $H_s = 0.45$ mm is used for this purpose, as its structure elements can be considered quasi-isolated from one another (see Sect. 3.3). To minimize distortions from weak

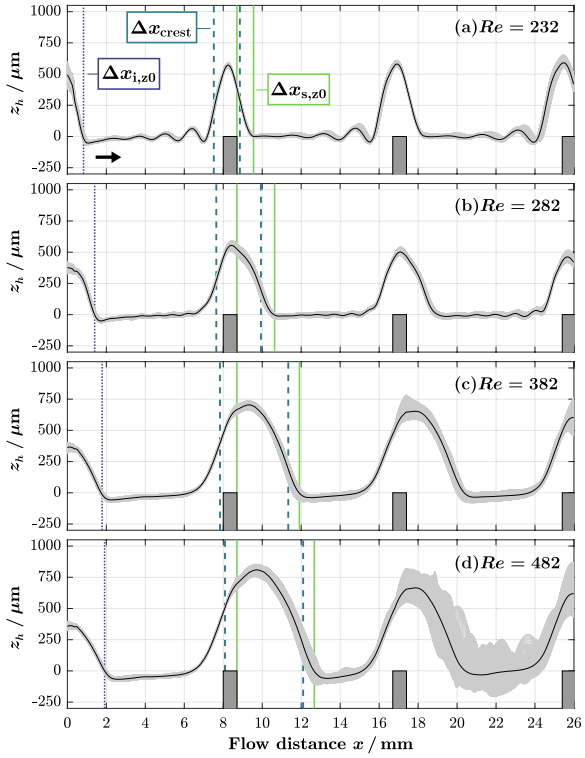

Fig. 13 Position of the gas–liquid interface $z_{\mathrm{h}}(x)$ for film flow over quasi-isolated structure elements ($D_{\mathrm{s}} = 8$ mm, $H_{\mathrm{s}} = 0.45$ mm) at different Reynolds numbers Re (a)–(d). The profiles determined for all individual spatial and temporal sample points (bright lines) are shown in addition to the overall spatio-temporal average (dark line). The extracted streamwise length scales are indicated by vertical lines

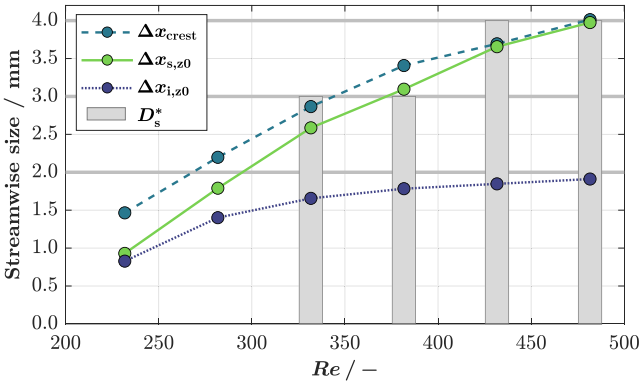

Fig. 14 Characteristic streamwise length scales as a function of Reynolds number Re for $D_{\mathrm{s}} = 8$ mm and $H_{\mathrm{s}} = 0.45$ mm. The ridge size at the initial step-down ($\Delta x_{\mathrm{i,z0}}$) is shown in addition to the ridge size in the vicinity of a structure element ($\Delta x_{\mathrm{s,z0}}$ and $\Delta x_{\mathrm{crest}}$). The definitions are visualized in Fig. 13a. Bars indicate the structure distances D_{s}^*, at which intensified interfacial oscillations were observed in our previous study (Düll et al. 2024). They were identified from a set of discrete structure distances $D_{\mathrm{s}} \in \{2, 3, 4, 6, 8\}$ mm (horizontal lines). No reliable values were available for the two lowest Re due to local dewetting

time-oscillatory interface motion or wall effects, the region of interest is restricted to the first few structure elements ($x = 0 - 26$ mm) and the central plate section in spanwise direction ($y = 20 - 30$ mm). It is marked by label (e) in Fig. 4. The extracted line profiles of the interface elevation $z_h(x)$ as a function of the flow distance x are depicted in Fig. 13a–d

for Reynolds numbers in the range of $Re = 282 - 482$. In the figures, the individual interface profiles, sampled at 158 discrete locations across the spanwise direction for eleven time instances with a time difference of 1s, are superimposed (bright lines). The overall spatio-temporal mean value is additionally indicated by a dark line.

For the two lowest investigated Reynolds numbers ($Re \leq 282$), a distinct tail of capillary ridges and depressions is visible upstream of each structure element (see Fig. 13a and b). These surface features are, however, damped with increasing Reynolds number, when the flow becomes inertia-dominated (see Fig. 13c and d). A similar behavior was theoretically predicted by Bontozoglou and Serifi (2008) for vertical falling film flow over a single step-up or step-down, and the critical Reynolds number for the disappearance of capillary features estimated based on data presented in their work ($Re \approx 220 - 250$) is in the same value range as that observed in our experimental study. The observed dominance of inertia forces aligns well with our findings on inertia-controlled liquid overshoot in Sect. 3.2.

In addition to the disappearance of capillary features, a general shift of the interfacial ridge to x-positions further downstream of the structure element, as well as a growth in its streamwise size, can be observed with increasing Reynolds number. To quantify the latter, three characteristic length scales are defined and extracted from the averaged line profiles. They are visualized in Fig. 13 as vertical lines, with labels shown in subplot (a). Length scale $\Delta x_{\mathrm{i,z0}}$ represents the flow distance required by the flow to penetrate into the trench after the first step-down ($z_h \to 0$, subscript 'z0') in direct vicinity of the liquid inlet (subscript 'i'). Length scale $\Delta x_{\mathrm{s,z0}}$ is defined in a similar manner but with respect to the downstream edge of a structure element (subscript 's'). Lastly, length scale $\Delta x_{\mathrm{crest}}$ also pertains to the interface deformation in the vicinity of a structure element, but its size is determined from the x-positions of maximal positive and negative interface slope (see also Fig. 11). A definition similar to the latter was previously employed to characterize the interface deformation at an isolated step-up or step-down (Bontozoglou and Serifi 2008). As can be taken from Fig. 14,

all three streamwise length scales increase with Reynolds number Re. However, while the streamwise size of the interfacial ridge after the initial step-down ($\Delta x_{\mathrm{i,z0}}$) appears to converge to a limiting value around 2 mm, the streamwise

size of the interfacial ridge induced in the vicinity of a quasi-isolated structure element ($\Delta x_{s,z0}$ or Δx_{crest}) continues to grow. Such a structure element represents a combination of a closely spaced step-up and step-down. For the inertia-dominated flow regime, this further emphasizes the significant influence of liquid overshoot in wall-normal direction at the structure element's upstream edge (step-up) on the overall flow behavior.

Regarding the optimization of surface structures for inducing strong interfacial oscillations, the streamwise length scale of the interfacial ridge at the initial step-down ($\Delta x_{s,z0}$) can be considered a limiting structure distance, below which the film flow is not expected to penetrate into the trenches between consecutive structure elements, resulting in reduced flow destabilization. The streamwise length scale of the interfacial ridge in the vicinity of a structure element ($\Delta x_{s,z0}$ or Δx_{crest}) is in good agreement with the optimal structure distance D_s^* from a discrete value set $D_s \in \{2, 3, 4, 6, 8\}$ mm, at which particularly intense interfacial oscillations were determined in our previous study (Düll et al. 2024). The latter are indicated in Fig. 14 in the form of bars. Thus, for the investigated rectangular corrugations with a structure height of $H_s = 0.45$ mm and a streamwise size of $L_s = 0.7$ mm, the streamwise length scale of the steady interface deformation at a single structure element can indeed serve as an estimate for the optimal spacing in an array of consecutive structure elements to induce significant transient flow destabilization.

4 Conclusion

Our contribution presents a spatio-temporal characterization of the evolution of transient interfacial waves in aqueous falling film flows over rectangular corrugations oriented perpendicular to the main flow direction. The associated flow destabilization is of high interest in the context of heat and mass transfer applications. To resolve the liquid film thickness distributions and associated wave characteristics in both space and time, the study relies on high-speed imaging and image processing based on an internally referenced light absorption method. An initial validation against measurements with a commercial chromatic confocal point sensor highlights the suitability of our customized experimental technique for capturing the highly dynamic flow properties. The validated method is subsequently employed to investigate the interconnection between steady and transient flow characteristics, aiming to elucidate how certain structure geometries induce particularly strong interfacial oscillations in the falling film. The experimental configuration and flow conditions are chosen to reflect those encountered in heat and mass transfer applications, with a focus on falling film absorbers for CO_2 capture. The main conclusions derived for this specific application case were discussed in detail in the previous section and are briefly summarized below.

In all experimental cases considered in this study, the transient film instabilities evolve from an initially steady surface deformation, with inertia-controlled liquid overshoot in wall-normal direction at the structure element's upstream edge playing a crucial role in the overall flow destabilization. A decomposition of the developed flow into its steady and time-oscillatory contributions reveals distinct spatial characteristics. While the former exhibits a dominant two-dimensional wave shape extruded in spanwise direction with a primary wavelength matching that of the bottom contour, the latter is significantly more isotropic in shape. Despite this, both steady and oscillatory flow contributions appear to be related, with particularly intense oscillatory motion typically observed when the underlying steady base film is strongly sloped. Three-dimensional steady wave patterns can be observed when the oscillation intensity is low; however, they are usually more localized effects.

A final comparison between the streamwise length scale of the steady interfacial ridge induced at quasi-isolated structure elements with a height of 0.45 mm and the corresponding optimal structure distance, at which particularly strong interfacial oscillations are induced in the film flow, reveals a good agreement between both values. In the context of surface structure optimization, this indicates that, for the specific structure geometry considered, characteristic length scales derived from steady interface deformations may serve as easily accessible predictors for optimized structure spacings that result in intense transient flow destabilization. In future work, more detailed experimental and theoretical analyses are needed to assess the validity of this observation for different experimental configurations, structure sizes and geometries, operating conditions, as well as for other working fluids with varying density, viscosity or surface tension. The latter is expected to have a particularly strong impact on low-Reynolds-number flows. Nevertheless, this initial finding not only emphasizes the interconnection between the steady and transient flow characteristics of aqueous falling film flows over corrugated surfaces, but also has the potential to accelerate the optimization of surface structures for enhancing the efficiency gas–liquid contactors in heat and mass transfer applications, such as falling film absorbers for CO_2 capture. More specifically, the observed relationship enables the estimation of suitable

structure spacings from a characteristic length scale that can be readily obtained through the analysis of steady film flows over isolated structure elements. As a consequence, the need for time-consuming screening experiments or computationally expensive transient flow simulations could be reduced.

Appendix A Sidewall effect

See Fig. 15.

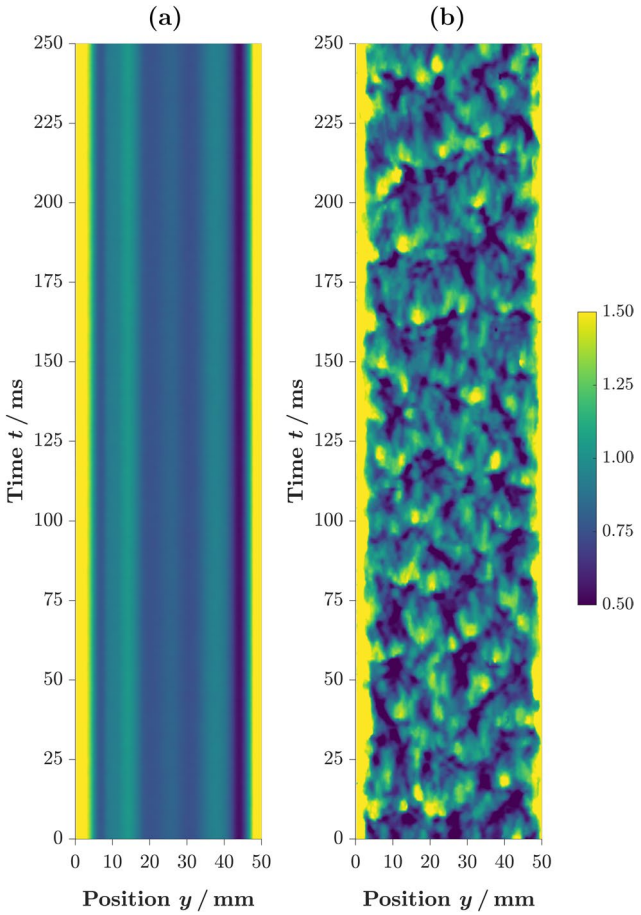

Fig. 15 Effect of sidewalls on the spatio-temporal wave evolution for falling film flow at $Re = 482$ over the smooth reference plate (**a**) and over a structured surface with $H_s = 0.45$ mm and $D_s = 4$ mm (**b**). The spanwise sampling line is positioned at a distance of $x \approx 100$ mm from the liquid distributor. The colormap indicates the local film thickness $h(y, t)$ normalized by the overall mean value $\overline{h}$ for each case. The sidewalls, which are responsible for the spanwise film thickness modulations in the case of the smooth plate, are located at $y = 0$ mm and $y = 50$ mm. Additional information on the sidewall effect can be found in our previous study (Düll et al. 2024)

Appendix B Illumination homogeneity

See Fig. 16.

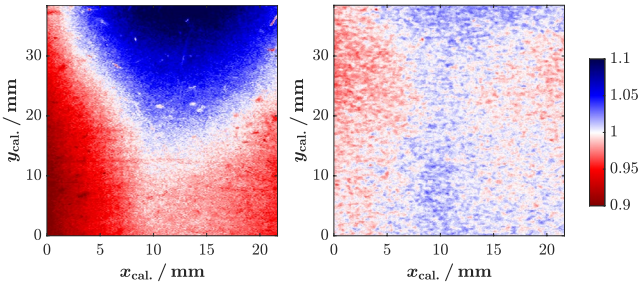

Fig. 16 Normalized intensity distribution $X/\overline{X}$ of the grayscale intensity ($X = I_{gray}$, subfigure **a**) and red-to-blue intensity ratio ($X = I_{red}/I_{blue}$, subfigure **b**) for the region of interest of an exemplary calibration image with constant liquid film thickness. The grayscale value is calculated from the light intensity captured by the camera's individual color channels: $I_{gray} = 0.299\, I_{red} + 0.587\, I_{green} + 0.114\, I_{blue}$

Appendix C Spatial and temporal flow statistics

See Fig. 17.

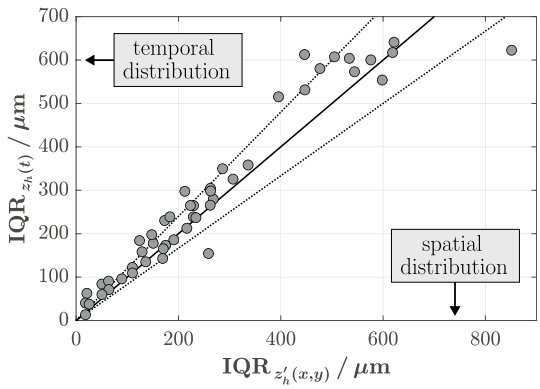

Fig. 17 Interquartile range IQR determined for the spatial distribution of the interface elevation's oscillatory contribution $z'_h(x, y)$ over the rectangular region of interest (**c**) in Fig. 4 at a single time instance (t = constant, abscissa) and for the temporal evolution of the interface elevation at the localized measurement point (**a**) in Fig. 4 (x, y = constant, ordinate). The IQR is a measure for the intensity of the interface motion. The solid and dashed lines represent the identity line and ±20% error limits. Results for all experimental cases considered in this study are shown. Local dewetting effects and associated liquid maldistribution can result in outliers

Appendix D Spatial gradient fields and derived properties

See Figs. 18, 19 and 20.

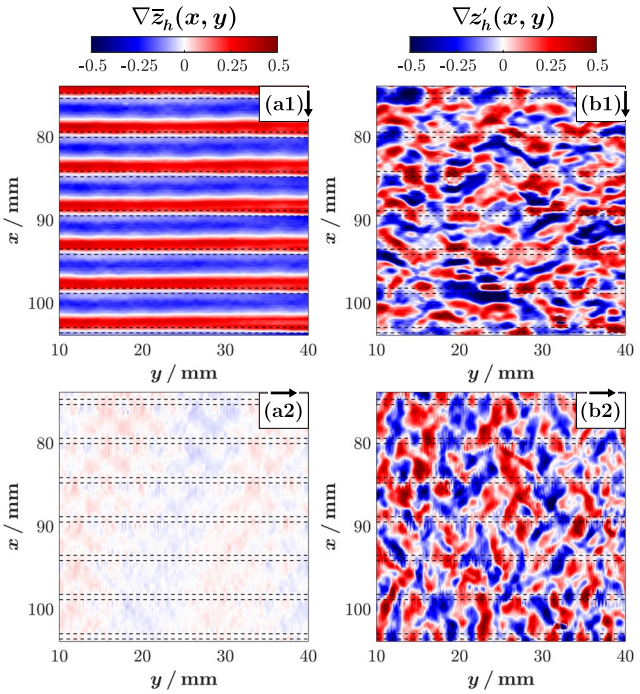

Fig. 18 Spatial gradient of the elevation of the gas–liquid interface in the streamwise direction x (number index 1) and the spanwise direction y (number index 2) for the region of interest (**c**) in Fig. 4. Results for the steady ($\nabla\bar{z}_h(x,y)$, letter index **a**) and for the oscillatory ($\nabla z'_h(x,y)$, letter index **b**) flow contributions are shown. $D_s = 4$ mm, $H_s = 0.45$ mm and $Re = 382$

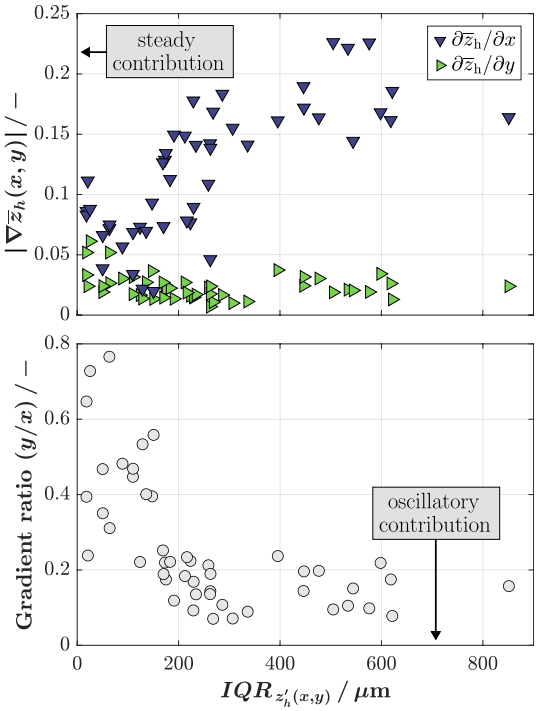

Fig. 19 Comparison of the strength of the oscillatory flow contribution ($IQR_{z'_h(x,y)}$) with **a** the absolute spatial gradients of the steady interface deformation ($|\nabla\bar{z}_h(x,y)|$) and with **b** the ratio of these gradients in spanwise (y) and streamwise (x) direction. Median values calculated over the region of interest (**c**) in Fig. 4 are shown for all experimental cases considered in this study

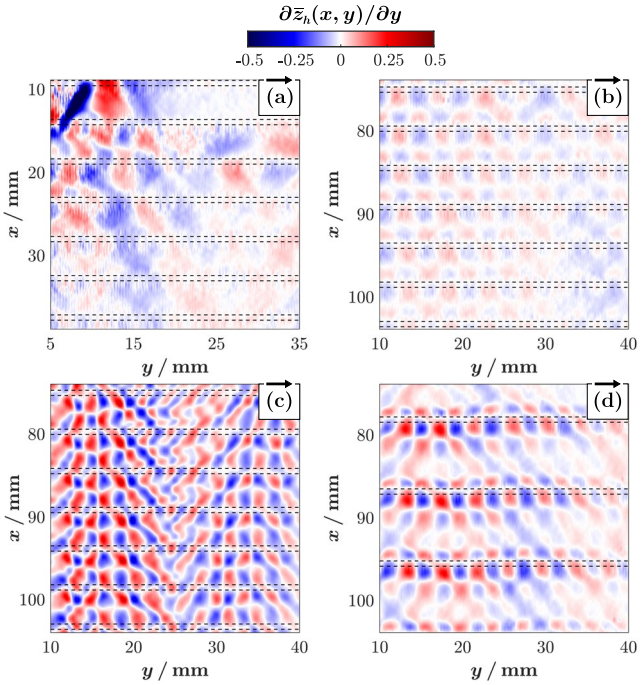

Fig. 20 Spanwise gradient $\partial \bar{z}_h / \partial y$ of the steady interface deformation for experimental cases where more pronounced steady three-dimensional wave patterns are observed. The figure indices (**a**–**d**) correspond to those from Fig. 12

Supplementary Information The online version contains supplementary material available at https://doi.org/10.1007/s00348-025-03978-2.

Acknowledgements The authors extend their sincere thanks to Imaging Solutions GmbH (https://imaging-solutions.de/) for providing the high-speed camera and a light source, as well as for their continuous technical support with the equipment. The authors also thank Prof. Hans-Jórg Bauer, Dr. Rainer Koch and M.Sc. Stefanos Melekidis (all from the Institute of Thermal Turbomachinery, KIT) for fruitful scientific discussions and for providing experimental equipment. Financial support by the Friedrich and Elisabeth Boysen Foundation (Project-ID Boy-165) and the Helmholtz program 'Materials and Technologies for the Energy Transition, Germany' (MTET, 38.03.04) is gratefully acknowledged.

Funding Open Access funding enabled and organized by Projekt DEAL.

Data availability The research data will be available at https://doi.org/10.35097/96bzfuq5g04ydneq.

Declarations

Conflict of interest The authors have no conflicts of interest to declare that are relevant to the content of this article.

Ethical approval Not applicable.

References

Åkesjö A, Gourdon M, Vamling L et al (2019) Modified surfaces to enhance vertical falling film heat transfer - an experimental and numerical study. Int J Heat Mass Transfer 131:237–251. https://doi.org/10.1016/j.ijheatmasstransfer.2018.11.061

Al-Shamaa B, Kahraman T, Wierschem A (2023) Steady three-dimensional patterns in gravity-driven film flow down an inclined sinusoidal bottom contour. Phys Fluids 35(3):033307. https://doi.org/10.1063/5.0140841

Al-Sibai F (2004) Experimentelle Untersuchung der Strömungscharakteristik und des Wärmeübergangs bei welligen Rieselfilmen. Dissertation, RWTH Aachen University, Retrieved from https://nbn-resolving.org/urn:nbn:de:hbz:82-20050535

Argyriadi K, Vlachogiannis M, Bontozoglou V (2006) Experimental study of inclined film flow along periodic corrugations: the effect of wall steepness. Phys Fluids 18(1):012102. https://doi.org/10.1063/1.2163810

Bontozoglou V, Serifi K (2008) Falling film flow along steep two-dimensional topography: the effect of inertia. Int J Multiphase Flow 34(8):734–747. https://doi.org/10.1016/j.ijmultiphaseflow.2008.01.006

Charogiannis A, Markides CN (2016) Application of planar laser-induced fluorescence for the investigation of interfacial waves and rivulet structures in liquid films flowing down inverted substrates. Interfac Phenom Heat Transfer 4(4):235–252. https://doi.org/10.1615/InterfacPhenomHeatTransfer.2017019587

Charogiannis A, Markides CN (2019) Spatiotemporally resolved heat transfer measurements in falling liquid-films by simultaneous application of planar laser-induced fluorescence (PLIF), particle tracking velocimetry (PTV) and infrared (IR) thermography. Exp Therm Fluid Sci 107:169–191. https://doi.org/10.1016/j.expthermflusci.2018.11.001

Charogiannis A, Sik An J, Voulgaropoulos V et al (2019) Structured planar laser-induced fluorescence (S-PLIF) for the accurate identification of interfaces in multiphase flows. Int J Multiphase Flow 118:193–204. https://doi.org/10.1016/j.ijmultiphaseflow.2019.06.002

Cherdantsev A, Bobylev A, Guzanov V et al (2023) Measuring liquid film thickness based on the brightness level of the fluorescence: Methodical overview. Int J Multiph Flow 168:104570. https://doi.org/10.1016/j.ijmultiphaseflow.2023.104570

Clark WW (2002) Liquid film thickness measurement. Multiph Sci Technol. https://doi.org/10.1615/MultScienTechn.v14.i1.10

Collignon R, Caballina O, Lemoine F et al (2021) Temperature distribution in the cross section of wavy and falling thin liquid films. Exp Fluids 62(5):115. https://doi.org/10.1007/s00348-021-03175-x

Cyklis P (2022) Effect of fouling on falling film evaporator performance in industrial conditions of fruit juice concentrate production. J Food Eng 317:110884. https://doi.org/10.1016/j.jfoodeng.2021.110884

Davies J, Warner K (1969) The effect of large-scale roughness in promoting gas absorption. Chem Eng Sci 24(2):231–240. https://doi.org/10.1016/0009-2509(69)80032-1

Düll A, Cros-Le Lagadec A, Buchmüller J et al (2024) Intensifying interfacial oscillations in falling film flows over rectangular corrugations. Phys Fluids 36(9):092107. https://doi.org/10.1063/5.0222760

Dupont J, Mignot G, Prasser HM (2015) Two-dimensional mapping of falling water film thickness with near-infrared attenuation. Exp Fluids 56(5):90. https://doi.org/10.1007/s00348-015-1955-1

Gourdon M, Innings F, Jongsma A et al (2015) Qualitative investigation of the flow behaviour during falling film evaporation of a dairy product. Exp Therm Fluid Sci 60:9–19. https://doi.org/10.1016/j.expthermflusci.2014.07.017

Guo YQ, Hong WR, Repke JU (2018) Hydrodynamics of new structured packings: an experimental and micro-scale cfd study. Microgravity Sci Technol 30(6):911–924. https://doi.org/10.1007/s12217-018-9648-z

Guzanov V, Bobylev A, Heinz O et al (2018) Characterization of 3-D wave flow regimes on falling liquid films. Int J Multiph Flow 99:474–484. https://doi.org/10.1016/j.ijmultiphaseflow.2017.11.013

Hann DB, Cherdantsev AV, Mitchell A et al (2016) A study of droplet impact on static films using the BB-LIF technique. Exp Fluids 57(4):46. https://doi.org/10.1007/s00348-016-2132-x

Havestini RA, Ormiston SJ (2020) An elliptic numerical analysis of water vapour absorption into a falling film in vertical parallel plate channels. Int J Heat Mass Transfer 150:119266. https://doi.org/10.1016/j.ijheatmasstransfer.2019.119266

Hu Z, Wang J, Dong H et al (2021) Hydrodynamics numerical simulation of a vertical falling film evaporator for ionic liquid systems. Chem Eng Sci 237:116563. https://doi.org/10.1016/j.ces.2021.116563

Imaging Solutions GmbH (2024) Constellation 120E Spektralkurve. https://imaging-solutions.eu/constellation120e/, Accessed 08 November 2024

Kapoustina V, Guffart J, Hien A et al (2019) Influence of a single microstructure on local mass transfer in liquid film flows. Chem Eng Res Des 146:352–362. https://doi.org/10.1016/j.cherd.2019.04.022

Lu Y, Stehmann F, Yuan S et al (2017) Falling film on a vertical flat plate - influence of liquid distribution and fluid properties on wetting behavior. Appl Therm Eng 123:1386–1395. https://doi.org/10.1016/j.applthermaleng.2017.05.110

Medina I, Scholl S, Rädle M (2022) Film thickness and glycerol concentration mapping of falling films based on fluorescence and near-infrared technique. Micromachines. https://doi.org/10.3390/mi13122184

Mendez M, Buchlin JM (2015) Dynamics of gas jet impingement on vertical falling liquid films. In: Proceedings of the 6th symposium of VKI PhD research (Rhode Saint Genese, Belgium

Mendez M, Németh L, Buchlin JM (2016) Measurement of liquid film thickness via light absorption and laser tomography. EPJ Web Conf 114:02072. https://doi.org/10.1051/epjconf/201611402072

Mortazavi M, Nasr Isfahani R, Bigham S et al (2015) Absorption characteristics of falling film LiBr (lithium bromide) solution over a finned structure. Energy 87:270–278. https://doi.org/10.1016/j.energy.2015.04.074

Mouza AA, Vlachos NA, Paras SV et al (2000) Measurement of liquid film thickness using a laser light absorption method. Exp Fluids 28:355–359. https://doi.org/10.1007/s003480050394

Njifenju AK, Bico J, Andrès E et al (2013) Experimental investigation of liquid films in gravity-driven flows with a simple visualization technique. Exp Fluids 54(5):1506. https://doi.org/10.1007/s00348-013-1506-6

Özgen S, Carbonaro M, Sarma GSR (2002) Experimental study of wave characteristics on a thin layer of de/anti-icing fluid. Phys Fluids 14(10):3391–3402. https://doi.org/10.1063/1.1501282

Prahl S (2017) Methylene blue spectra. https://omlc.org/spectra/mb/, Accessed 15 Mar 2024

Qi R, Dong C, Zhang LZ (2019) Wave-wise falling film in liquid desiccant dehumidification systems: Model development and time-series parameter analysis. Int J Heat Mass Transfer 132:96–106. https://doi.org/10.1016/j.ijheatmasstransfer.2018.11.150

Rößler H, Wiesenhofer W, Glasmacher-Remberg C, et al. (2013) Thin-film reactors. In: Ullmann's encyclopedia of industrial chemistry. Wiley-VCH, Weinheim

Saliba GC, Korvink JG, Brandner JJ (2024) Magnetic resonance velocimetry reveals secondary flow in falling films at the microscale. Phys Fluids 36(7):071705. https://doi.org/10.1063/5.0214609

Sayegh MA, Rouzineau D, Meyer M et al (2022) Impact of physicochemical properties on falling liquid films flow over flat and corrugated surfaces. Int J Multiphase Flow 155:104170. https://doi.org/10.1016/j.ijmultiphaseflow.2022.104170

Schagen A (2014) Methode der laser-induzierten Lumineszenz zur experimentellen Analyse des Stofftransportes in laminar-welligen Flüssigkeitsfilmen. Dissertation, RWTH Aachen University, Retrieved from https://nbn-resolving.org/urn:nbn:de:hbz:82-rwth-2015-021913

Schörner M (2018) The stability of gravity-driven viscous films over topography. Dissertation, Universität Bayreuth, Retrieved from https://nbn-resolving.org/urn:nbn:de:bvb:703-epub-3855-4

Schröder T (2019) Strömungscharakteristika und Wärmeübertragung eines angeregten Fallfilms. Dissertation, TU Darmstadt, Retrieved from https://nbn-resolving.de/urn:nbn:de:tuda-tuprints-87427

Vlachogiannis M, Bontozoglou V (2002) Experiments on laminar film flow along a periodic wall. J Fluid Mech 457:133–156. https://doi.org/10.1017/S0022112001007637

Wagner W, Kretzschmar HJ (2013) Wasser. In: VDI e.V. (ed) VDI-Wärmeatlas. Springer Vieweg, Berlin, Heidelberg, chap D2.1, p 176

Wierschem A, Scholle M, Aksel N (2003) Vortices in film flow over strongly undulated bottom profiles at low Reynolds numbers. Phys Fluids 15(2):426–435. https://doi.org/10.1063/1.1533075

Zadrazil I, Markides CN (2014) An experimental characterization of liquid films in downwards co-current gas–liquid annular flow by particle image and tracking velocimetry. Int J Multiph Flow 67:42–53. https://doi.org/10.1016/j.ijmultiphaseflow.2014.08.007

Zadrazil I, Matar OK, Markides CN (2014) An experimental characterization of downwards gas-liquid annular flow by laser-induced fluorescence: flow regimes and film statistics. Int J Multiph Flow 60:87–102. https://doi.org/10.1016/j.ijmultiphaseflow.2013.11.008

Zanfir M, Gavriilidis A, Wille C et al (2005) Carbon dioxide absorption in a falling film microstructured reactor: experiments and modeling. Ind Eng Chem Res 44(6):1742–1751. https://doi.org/10.1021/ie049726k

Zhang F, Guo L, Ding Y et al (2018) Flow pattern and co2 absorption in a falling film reactor with mixed aqueous solution of ionic liquid and MEA. Appl Therm Eng 138:583–590. https://doi.org/10.1016/j.applthermaleng.2018.04.041

Zhao Y, Markides CN, Matar OK et al (2013) Disturbance wave development in two-phase gas–liquid upwards vertical annular flow. Int J Multiphase Flow 55:111–129. https://doi.org/10.1016/j.ijmultiphaseflow.2013.04.001

Zhou D, Gambaryan-Roisman T, Stephan P (2009) Measurement of water falling film thickness to flat plate using confocal chromatic sensoring technique. Exp Therm Fluid Sci 33(2):273–283. https://doi.org/10.1016/j.expthermflusci.2008.09.003